



An insight into the adsorption and photocatalytic degradation of rhodamine B in periodic mesoporous materials

Shivatharsiny Rasalingam, Rui Peng, Ranjit T. Koodali*

Department of Chemistry, University of South Dakota, Vermillion, SD 57069, USA

ARTICLE INFO

Article history:

Received 2 December 2014

Received in revised form 10 February 2015

Accepted 27 February 2015

Available online 28 February 2015

Keywords:

Adsorption
Mesoporous
Rhodamine B
Degradation
Tetrahedral

ABSTRACT

The present study explores the different modes of adsorption of rhodamine B dye over two different siliceous (Si-MCM-48 and Si-MCM-41) and titania loaded siliceous (Ti-MCM-48 and Ti-MCM-41) mesoporous materials. The equilibrium adsorption studies indicate that siliceous as well as Ti-loaded mesoporous materials are good adsorbents for the removal of rhodamine B dye from aqueous solutions, and an enhanced uptake was obtained with siliceous than the titania loaded mesoporous materials. The adsorption data were fitted with different isotherms, and it was observed in general that the dye molecules obeyed Langmuir type of adsorption. The presence of rhodamine B dimer was evident from DRS analysis, and the J-dimer formation of rhodamine B molecules was proved by photoluminescence (PL) studies. In addition, the degradation of rhodamine B dye over titania loaded and siliceous mesoporous materials indicate that Ti-MCM-41 is more effective than Ti-MCM-48, whereas only decoloration of the dye was observed in both of the siliceous materials. Furthermore, Ti^{4+} in tetrahedral coordination plays a vital role in enhancing the degradation efficiency, and the degraded products were identified by using electrospray ionization-mass spectrometry (ESI-MS) studies.

© 2015 Elsevier B.V. All rights reserved.

1. Introduction

Organic dyes find application in several industries, including textile, paper, pigment, food, cosmetic, and drug manufacturing [1]. The extensive use of organic dyes and their indiscriminate disposal leads to serious environmental hazards. Dyes discharged from industries mainly cause water contamination and pose threat to public hygiene, health, and environment, since some of the dyes and their metabolites are toxic, carcinogenic, mutagenic, or teratogenic [2]. Hence, the elimination of dyes from wastewater is of vital significance.

A number of approaches, such as electro-oxidation [3], ozonation [4], electro-kinetic coagulation [5], ion-exchange [6], membrane filtration [7], microbial degradation [8] etc., have been developed to remove dyes [9]. However, these methods are either expensive or lack efficiency. Hence, economic and cost-effective methods need to be explored for the removal of dyes. Adsorption has been suggested as an affordable strategy for the removal of different types of dyes. Adsorbents, such as activated carbon [10,11], peat [12], wood chips [13], fly ash, coal [14], clay [15], chitosan [16–18] etc., have been explored and reported in the literature. High surface area is one of the primary requirements considered

for a good adsorbent. M41S ordered mesoporous materials, owing to its high surface area, uniform pore size, and high pore volume, have been used as ideal candidates to adsorb dye molecules. Since their discovery in 1992 [19,20], M41S mesoporous materials have attracted immense interest due to their versatile applications in various fields [21]. Among the various classes of mesoporous materials, the hexagonal forms, MCM-41 and SBA-15 materials have been extensively studied for various applications, including adsorption and/or mineralization of dyes, such as methylene blue, rhodamine B [22–29], tectilon blue [30], crystal violet [31], basic yellow 87 [32] etc. Another important class of mesoporous material is the cubic MCM-48 material. MCM-48 is attractive as a catalyst and as an adsorbent, since it has a three-dimensional inter-penetrating network of pores that helps in effective diffusion of molecules. The 3-D pore geometry reduces pore clogging that frequently occurs in uni-dimensional mesoporous materials, such as MCM-41 and SBA-15. However, the use of MCM-48 materials as adsorbents for dye molecules is limited mainly due to the inherent challenges in the synthesis of MCM-48 [23,33]. Most importantly, literature reports regarding degradation of dyes over MCM-41 and/or MCM-48 materials are limited and there are conspicuous gaps in knowledge [34–38]. There are no literature reports that have examined the adsorption and photocatalytic degradation of rhodamine B over titania loaded cubic MCM-48 mesoporous materials.

* Corresponding author. Tel.: +1 605 677 6189; fax: +1 605 677 6397.
E-mail address: Ranjit.Koodali@usd.edu (R.T. Koodali).

Photocatalytic degradation is an effective removal technique that takes place in the presence of reactive oxidative species, such as $\bullet\text{OH}$, $\bullet\text{OOH}$, H_2O_2 , etc. Moreover, photocatalytic degradation helps in the conversion of the toxic pollutants to relatively non-toxic form, while adsorption only transfers the adsorbate from one phase to another. Therefore, it is imperative to evaluate the adsorption and the degradation ability of dyes over mesoporous materials. Notably, to the best of our knowledge only one literature report has compared the photocatalytic activity of anionic and cationic dyes over transition metal oxide loaded MCM-41 and MCM-48 materials. Even though the activity of these materials were compared with commercial TiO_2 catalyst, a structure-activity relationship was not demonstrated in their study and hence, the critical factors responsible for the differences in the photocatalytic activities still seems unclear [37]. Thus, existing literature lacks: (i) a systematic and comprehensive characterization of physico-chemical properties of periodic mesoporous materials with regards to adsorption and photocatalytic degradation, (ii) detailed and comparative investigation of adsorption of a hybrid model dye, such as rhodamine B over a uni-dimensional and three-dimensional periodic mesoporous MCM-41 and MCM-48 materials, (iii) exhaustive identification of the reaction intermediates and photodegradation products by mass spectrometric techniques, and (iv) elucidation of a structure-activity relationship to identify the factors responsible for photocatalytic degradation of dyes over titania loaded periodic mesoporous materials. Hence, it is important to evaluate the applicability of mesoporous materials toward environmental remediation applications, and understand the key factors responsible for adsorption and photocatalytic activity.

We have developed a rapid and facile method for the preparation of MCM-48 materials and demonstrated that the cubic form with its three-dimensional network of pores is an active catalyst compared to the uni-dimensional pores available in MCM-41 [39,40]. This work focuses on the synergism between adsorption and degradation of a hybrid dye, rhodamine B, over MCM-48 and MCM-41 materials. The factors responsible for enhanced adsorption (high surface area, larger pore volume, and difference in the surface charges etc.) have been systematically elucidated and identified in this work.

In general, the photocatalytic degradation of dye is improved when it is efficiently adsorbed on a catalyst. The larger, the amount of dye adsorbed on a catalyst, better is the chance to be degraded photocatalytically. Thus, a detailed understanding and in-depth study of photocatalytic degradation over adsorbents, such as, Ti-MCM-48 and Ti-MCM-41 was carried along with the Si-MCM-48 and Si-MCM-41 materials. A relatively high amount of titania (Si/Ti ratio of 10) was selected for preparing titania loaded MCM catalysts. It was found that the coordination of the Ti^{4+} species is the key for photocatalytic degradation, whereas the surface area, pore volume, and the surface charges play a pivotal role in the adsorption of rhodamine B. Furthermore, the detailed mechanism for rhodamine B dye degradation is investigated herein from electrospray ionization-mass spectrometry (ESI-MS) analysis. Thus, this work will bridge the gap in literature by providing new insights regarding the role of the coordination of Ti^{4+} species on the photocatalytic degradation of rhodamine B on periodic mesoporous materials.

2. Materials and methods

2.1. Materials

Tetraethyl orthosilicate (TEOS, 98%) and titanium(IV) isopropoxide was obtained from Acros. Cetyltrimethylammonium bromide (CTAB, 98%) and rhodamine B were purchased from Alfa. Ammonium hydroxide (NH_4OH) was obtained from Fisher. Ethanol

(200 Proof) was produced by Pharmo-AAPER. Deionized water was used throughout this study unless otherwise indicated. All the chemicals were used without further purification unless otherwise specified.

2.2. Synthesis of adsorbents

2.2.1. Si-MCM-48

The cubic siliceous mesoporous material was prepared as follows: 1.2 g of CTAB was added to 50 mL of deionized water in a plastic bottle and stirred vigorously. After the complete dissolution of the surfactant, 25 mL of ethanol was poured into the clear solution. Then, 6 mL of NH_4OH was added to the surfactant solution and finally 1.8 mL of TEOS was added. The suspension was stirred at 300 rpm for 4 h at room temperature. The powder was recovered by filtration, washed with water, and then dried in an oven at 80–90 °C overnight. The dried powder was then ground and calcined at 550 °C for 6 h in air to remove the surfactant.

2.2.2. Ti-MCM-48

Titania loaded MCM-48 material (Ti-MCM-48-10) was prepared as stated above excepting that the required amount of titanium(IV) isopropoxide was added to the surfactant solution to obtain Si/Ti ratio of 10 [41].

2.2.3. Si-MCM-41

1.5 g of CTAB was added to 30 mL of deionized water in a plastic bottle under vigorous stirring. After obtaining a clear colorless solution, 70 mL of aqueous NH_3 and 45 mL of ethanol were added into the clear solution. After 30 min of stirring, 3 mL of TEOS was added and suspension was stirred at 500 rpm for 3 h at room temperature. Then the stirring rate was maintained at 300 rpm for 12 h. The resultant powder was recovered by filtration, washed with water, and dried in an oven at 80–90 °C overnight. Finally, the dried powder was ground and calcined at 550 °C for 6 h in air to remove the surfactant.

2.2.4. Ti-MCM-41

Ti-MCM-41 was prepared as stated above with an additional step of adding an appropriate amount of titanium(IV) isopropoxide to obtain Si/Ti ratio of 10 (Ti-MCM-41-10).

2.3. Characterization

The XRD patterns were recorded on Rigaku Ultima IV using $\text{Cu K}\alpha$ radiation of wavelength 1.540806 Å. The conditions for XRD were as follows: voltage = 40 kV, current = 44 mA, step width = 0.02°, and scan rate = 1°/min. N_2 isotherms were performed on Quantachrome Nova 2200e analyzer at 77 K. The mesoporous materials were degassed extensively at 100 °C prior to adsorption measurements. The specific surface areas were determined by applying the Brunauer–Emmett–Teller (BET) equation in the relative pressure range of $P/P_0 = 0.05$ –0.30. The pore volume was determined by measuring the amount of nitrogen adsorbed at the highest relative pressure of $P/P_0 = 0.98$. The pore diameter was determined by applying the Barrett–Joyner–Halenda (BJH) equation to the desorption isotherm. DR spectra were acquired using a Cary 100 Bio UV–visible spectrophotometer with Harrick Scientific accessory. For DRS studies, a small amount of sample (dried overnight in an oven at 80–90 °C) was placed in the sample holder and the spectra were acquired in the wavelength range of 200–700 nm. Si-MCM-41 and Si-MCM-48 were used as reference to record the DR spectra of Ti-MCM-41-10 and Ti-MCM-48-10. Zeta potential measurements of the mesoporous materials were carried out using a Malvern Zetasizer NanoZS-90 equipped with a MPT2

titrator. The suspension concentration was kept at 1 mg/mL. Photoluminescence measurements of the dye-adsorbed mesoporous materials were conducted using a Horiba Jobin Yvon Fluoromax 4 instrument. About 5 mg of the sample was mixed thoroughly with 20 mg of KBr and a pellet was prepared. This pellet was inserted in the instrument and an excitation wavelength of 420 nm was used. The emission from the sample was scanned in the range of 450–750 nm.

2.4. Adsorption studies

Rhodamine B was employed for evaluating the adsorption capacity of four different mesoporous materials, namely Si-MCM-48, Ti-MCM-48-10, Si-MCM-41, and Ti-MCM-41-10. In a typical procedure, 20 mg of the adsorbent was added to 20 mL of the dye solution with known initial concentrations (ranging from 1×10^{-5} M to 50×10^{-5} M) in an amber colored reagent bottle. The bottle was covered by aluminum foil in order to prevent the exposure of light, and the suspension was stirred in the dark for 15 h. The suspension was then centrifuged and the absorption spectra of the supernatant solution were collected using a Cary 100 Bio UV–vis spectrophotometer. The equilibrium concentrations of rhodamine B were determined by monitoring the absorbance at the maximum wavelength ($\lambda_{\text{max}} = 554$) in relation to a previously prepared calibration plots.

The equilibrium adsorption capacity q_e (mol g^{-1}) was calculated using: $q_e = (C_0 - C_e)V/m$ where C_0 is the initial concentration of the dye solution (mol L^{-1}), C_e is the equilibrium concentration (mol L^{-1}), V

is the volume of the dye solution (mL), and m is the adsorbent mass (mg). Other equations relevant to the determination of the maximum amount of adsorption (q_m) are provided in the Supplementary information.

2.5. Photocatalysis

Photocatalytic degradation of rhodamine B was conducted as follows: 50 mg of photocatalyst was dispersed in 50 mL of 10×10^{-5} M rhodamine B solution, which was prepared in optima grade water (initial pH 6–7). The suspension was placed in a quartz cylindrical jacket reactor and stirred in the dark at 300 rpm for 15 h to establish adsorption–desorption equilibrium. Then, visible light was supplied by a Xenon arc lamp (Newport 1000 W) through a Pyrex glass filter (cut off 420 nm) with the applied light intensity of $\sim 98 \text{ mW cm}^{-2}$. The reaction temperature was maintained at $25 \pm 2^\circ \text{C}$ by channeling water in-between the walls of the reactor throughout the course of the experiment.

Four milliliter of the suspension (containing both the photocatalyst and rhodamine B solution) was withdrawn after 30 min, 60 min, 120 min, 180 min, 300 min, 420 min, and 600 min of irradiation. The suspension was centrifuged at 3200 rpm for 30 min and the clear supernatant was analyzed using UV–vis spectroscopy. The apparent rate constants (k_{app}) for the photocatalytic degradation was obtained assuming pseudo-first order kinetics and using the equation $(C/C_0) = e^{-k_{\text{app}}t}$, where C = concentration of the rhodamine B after irradiation for a certain time interval, C_0 = concentration of rhodamine B in the solution after adsorption for 15 h in the dark

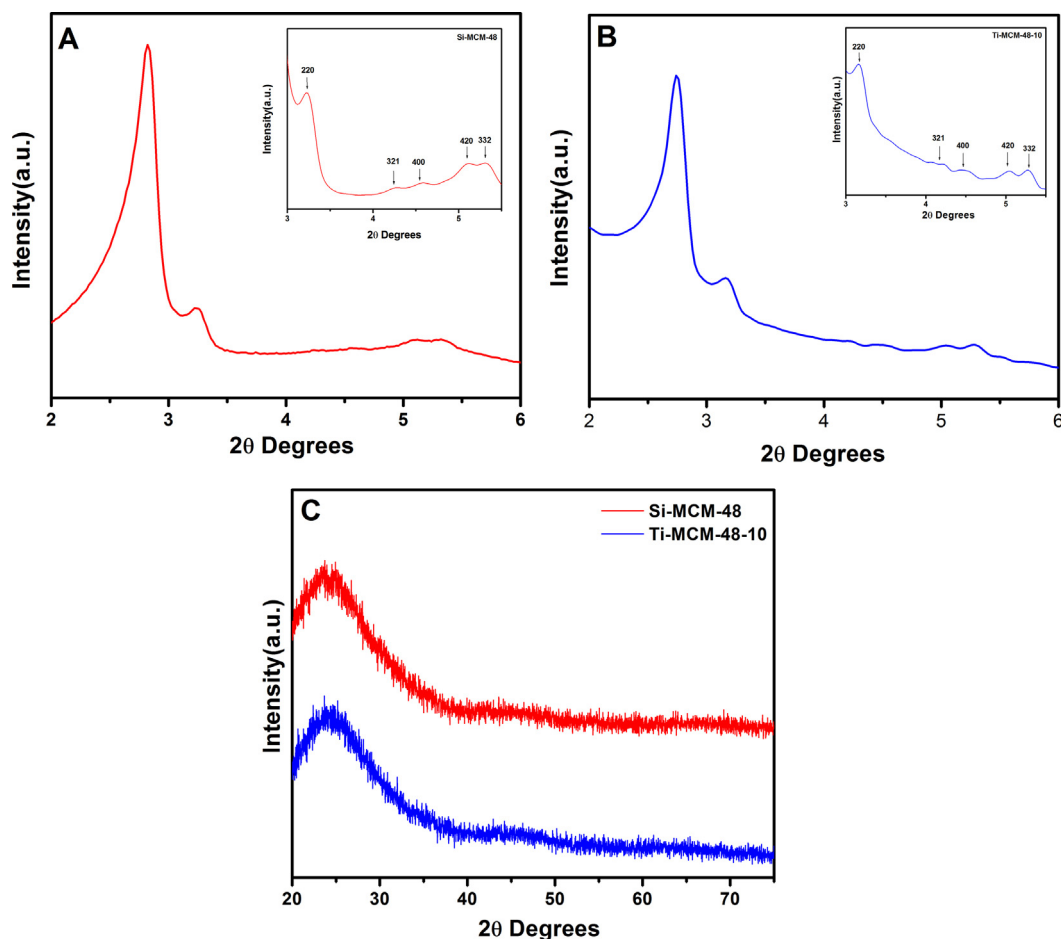


Fig. 1. Low angle Powder X-ray diffraction patterns of (A) Si-MCM-48, (B) Ti-MCM-48-10, and (C) high angle powder X-ray diffraction patterns of Si-MCM-48 and Ti-MCM-48-10.

and before irradiation, k_{app} = apparent rate constant, and t is the time of irradiation.

The obtained supernatant in different time intervals was then filtered over 0.45 micron filter. The filtrate were diluted ten times in volume ratio of 1:1 with optima grade methanol and water mixture. The resultant solution was introduced into the ESI source of the Varian 500-MS ion trap mass spectrometer for product analysis. The ionization was completed using a ESI source in positive mode to separate the fragments on the basis of their mass to charge ratio (m/z). The test samples were infused at the rate of $10 \mu\text{L min}^{-1}$, whereas the other parameters were kept as follows: spray shield voltage = 600 V, capillary voltage = 80 V, needle voltage = 5000 V, drying gas temperature = 400°C , nebulizer pressure = 10 psi, and the electron multiplier voltage = 1360 V. The peak patterns were recorded in the m/z range of 50–500.

3. Results and discussion

3.1. Powder XRD

Fig. 1A and B shows the low angle XRD patterns of Si-MCM-48 and Ti-MCM-48-10. Both samples show the characteristic Bragg reflections that are typical of cubic MCM-48 mesoporous materials. The insets in Fig. 1A and B show peaks due to d spacings ([220], [321], [400], [420], and [332]) that indicate an excellent periodically arrayed mesoporous structure. Compared to Si-MCM-48, Ti-MCM-48-10 shows lower peak intensity due to [211], [220],

[321], [400], [420], and [332] planes. The decrease in intensity could be ascribed to a weakening in the scattering contrast between the pores and pore walls due to the high loading of titania in the pores of MCM-48. The titania loading inside the pores of silica materials were further supported by TEM analysis (Fig. S1). It can be clearly seen from Fig. S1B that the dark spots (TiO_2) are well dispersed in the silica matrix. Fig. 1C exhibits the high angle XRD patterns and both samples show a broad peak ascribed to amorphous silica. No peaks due to bulk TiO_2 could be found in Ti-MCM-48-10. This may also be attributed to the high dispersion of the titania species in the MCM-48 mesoporous material. It is also possible that the titania species are amorphous and are present as small particles ($<3 \text{ nm}$) in the mesoporous matrix. The XRD instrument is not sensitive to the detection of small particles of titania ($<3 \text{ nm}$). Likewise, the low angle XRD patterns of Si-MCM-41 and Ti-MCM-41-10 are depicted in Fig. 2A and B.

The characteristic Bragg reflections for the MCM-41 mesoporous materials were observed at $2\theta \sim 2.6^\circ$, 4.4° , and 5.1° due to d spacings [100], [110], and [200], respectively, indicating the periodic nature of the materials. In addition, the periodic nature is retained after the incorporation of relatively large amounts of titania. The high angle XRD patterns of both the MCM-41 materials in the Fig. 2C shows a similar pattern as that of the MCM-48 materials; a broad peak due to silica can be observed. As discussed above for the MCM-48 materials, no peaks were observed due to TiO_2 in the long range scan thereby confirming the good dispersion of TiO_2 in the silica matrix. This is also evident from the TEM analysis (Fig. S2).

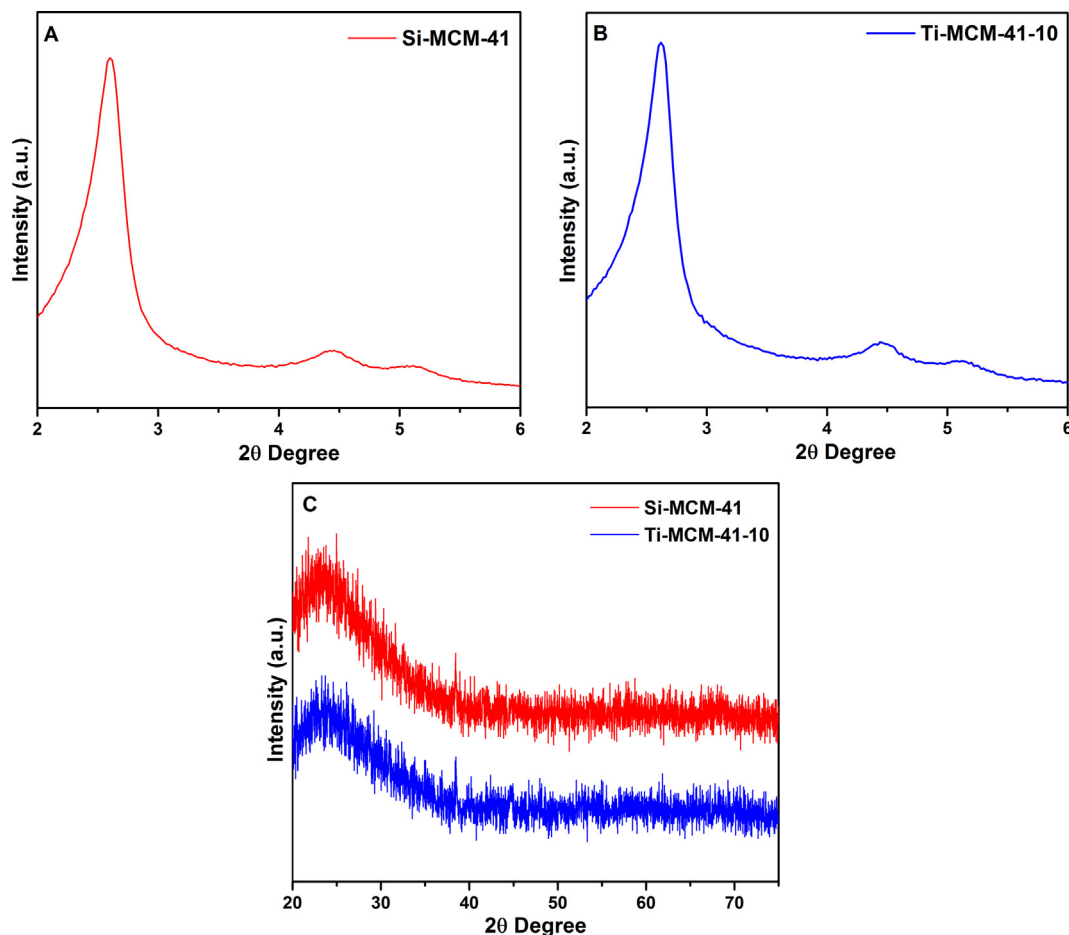


Fig. 2. Low angle Powder X-ray diffraction patterns of (A) Si-MCM-41, (B) Ti-MCM-41-10, and (C) high angle powder X-ray diffraction patterns of Si-MCM-41 and Ti-MCM-41-10.

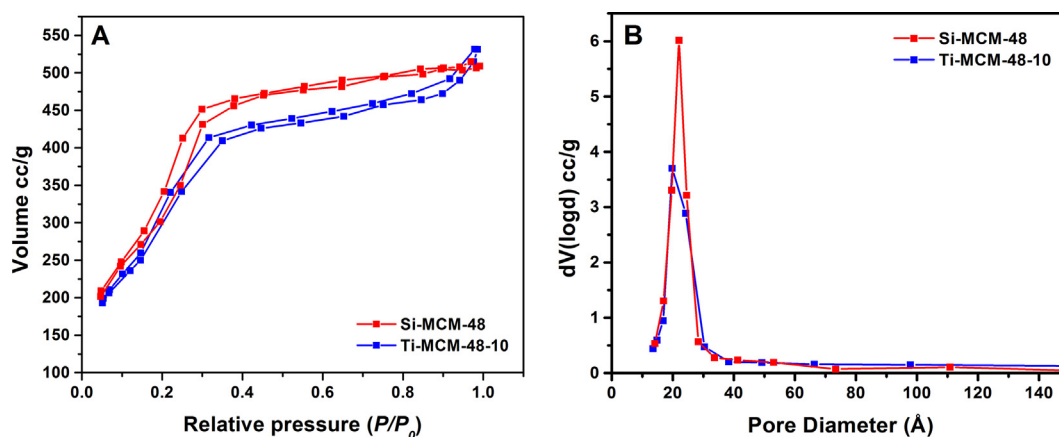


Fig. 3. (A) Nitrogen adsorption–desorption isotherms of Si-MCM-48 and Ti-MCM-48-10 and (B) pore size distribution of Si-MCM-48 and Ti-MCM-48-10.

3.2. N_2 isotherm

The adsorption isotherms of the materials were recorded using nitrogen as the carrier gas. Fig. 3A shows the nitrogen isotherms of Si-MCM-48 and Ti-MCM-48-10 materials. A standard type IV classification typical of mesoporous materials was observed for both samples. Initially, monolayer adsorption takes place, followed by multilayer adsorption. Subsequently, capillary condensation, which is implied by the steep inflection, appears at relative pressure (P/P_0) values between 0.2 and 0.4. This inflection reflects the mesoporosity present in the samples. Both isotherms show inflections at similar relative pressures and the sharpness of these steep inflections seem identical. The pore size distribution plots are depicted in Fig. 3B. Both the plots demonstrate uni-modal distribution of pores and suggest highly uniform pore sizes. The surface areas of the MCM-48 materials are greater than $1200 \text{ m}^2/\text{g}$ and decreases on loading with titania, consistent with our previous observations [40]. The pore volume of Ti-MCM-48 was found to be $0.82 \text{ cm}^3/\text{g}$ and lower than that of Si-MCM-48 ($1.03 \text{ cm}^3/\text{g}$) indicating that the titania particles are mostly located inside the pores. In addition, there is a slight decrease in the pore diameter from 22 Å to 20 Å for the samples Si-MCM-48 and Ti-MCM-48-10, respectively, indicating that the titania particles are well dispersed and are located within the pores. A similar behavior was observed with the MCM-41 materials and the nitrogen isotherms and pore size distribution of MCM-41 materials are illustrated in Fig. 4.

The surface area of Si-MCM-41 ($1453 \text{ m}^2/\text{g}$) was similar to that of Si-MCM-48. The surface area of Ti-MCM-41-10 material

Table 1

Textural properties, amount adsorbed, and the degradation rate of the mesoporous materials.

Samples	SA (m^2/g)	PV (cm^3/g)	PD (Å)	q_m (mol/g)	Overall rate (min^{-1})
Si-MCM-41	1453	0.79	22.0	8.2×10^{-4}	–
Ti-MCM-41-10	1303	0.75	22.0	4.1×10^{-4}	4.55×10^{-3}
Si-MCM-48	1457	1.03	22.0	8.5×10^{-4}	–
Ti-MCM-48-10	1219	0.82	20.0	4.6×10^{-4}	3.17×10^{-3}

SA refers the surface area of the materials and determined by applying Brunauer–Emmett–Teller (BET) equation to a relative pressure (P/P_0) range of 0.05–0.30 to the adsorption isotherm. PV refers to pore volume and is calculated from the amount of nitrogen adsorbed at the highest relative pressure (P/P_0) ~ 0.98 . PD refers to pore diameter, and was calculated from the Barrett–Joyner–Halenda (BJH) equation using the desorption isotherm. q_m refers to the maximum amount of rhodamine B adsorbed.

($1303 \text{ m}^2/\text{g}$) was lower in comparison to that of Si-MCM-41. The pore volume of both the MCM-41 materials was lower compared to the MCM-48 materials. The textural properties of the samples, the maximum amount of rhodamine B dye adsorbed on the materials, and the degradation rate constant of rhodamine B dye on the TiO_2 loaded materials are listed in Table 1.

3.3. UV–vis diffuse reflectance spectroscopy (DRS)

Fig. 5A shows the de-convoluted DRS spectrum of Ti-MCM-48-10 sample. The peak observed at 220 nm is assigned to Ti^{4+} in tetrahedral coordination and is due to the ligand-to-metal charge-transfer (LMCT) from O^{2-} to Ti^{4+} . The presence of this peak is

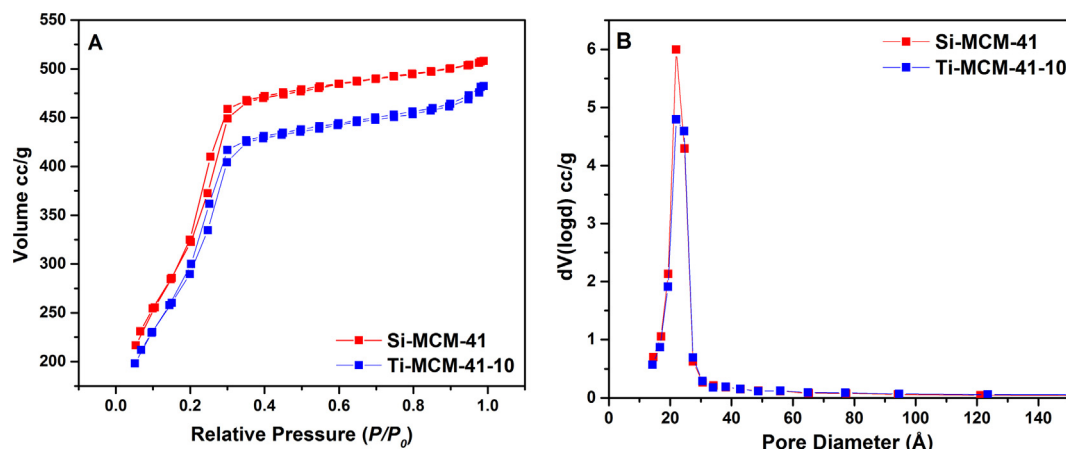


Fig. 4. (A) Nitrogen adsorption–desorption isotherms of Si-MCM-41 and Ti-MCM-41-10 and (B) pore size distribution of Si-MCM-41 and Ti-MCM-41-10.

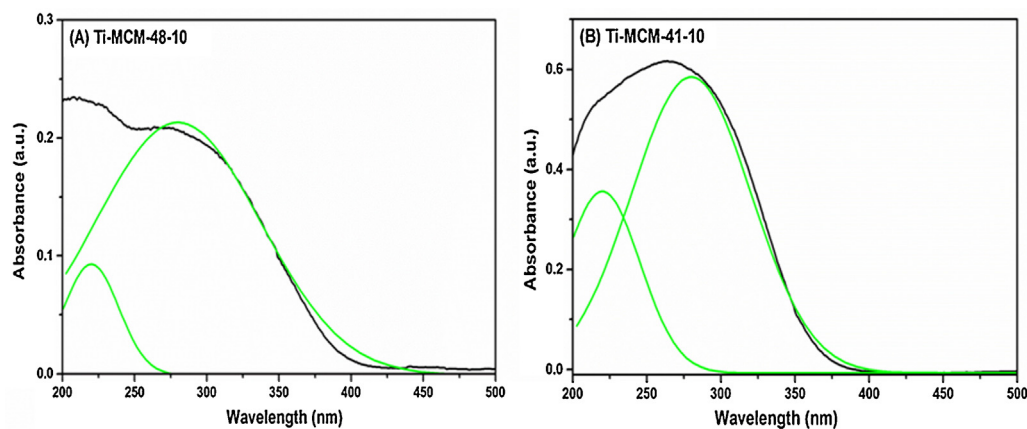


Fig. 5. De-convoluted diffuse reflectance spectra of (A) Ti-MCM-48-10 sample and (B) Ti-MCM-41-10.

also an indication that the Ti^{4+} species are fairly isolated and well dispersed in the MCM-48 silica framework. An additional band at 280 nm was also observed, which could be typically assigned to Ti^{4+} ions in octahedral coordination. Hence, we can conclude that most of the Ti^{4+} ions are octahedrally coordinated and a small portion of Ti^{4+} ions are tetrahedrally coordinated in the Ti-MCM-48-10 mesoporous material. In contrast to the peak pattern of Ti-MCM-48, a broad peak was detected with the Ti-MCM-41-10 material (Fig. 5B), which also indicates the presence of both tetrahedral and octahedral Ti^{4+} species in the material. To obtain the relative ratio of tetrahedral and octahedral coordination of Ti^{4+} species in Ti-MCM-48 and Ti-MCM-41 materials, the peaks obtained from the DRS analysis were de-convoluted using Origin Pro 9.0 software. The peak centers were fixed at 280 and 220 nm for the octahedral and tetrahedral geometry of Ti^{4+} species, respectively. The relative ratios of Ti^{4+} species in octahedral and tetrahedral coordination was estimated by calculating the peak intensity from the baseline to the top of the peak center with a fixed width at wavelengths 220 ± 5 nm and 280 ± 5 nm, respectively. The ratio of octahedral/tetrahedral was found to be 2.38 and 1.65 for Ti-MCM-48-10 and Ti-MCM-41-10 materials, respectively.

3.4. Adsorption studies

The adsorption efficiency of rhodamine B on the different mesoporous adsorbents were modeled using three popular isotherms (*i.e.*, Langmuir, Freundlich, and Redlich–Peterson) in

this work. Fig. 6 illustrates the non-linear fit for Si-MCM-48 and Ti-MCM-48-10. The equations employed in fitting the data using the three isotherms are described in the Supplementary information section. The best-fit isotherm was resolved from the experimental correlation coefficient value, R^2 , listed in Table S1. The data in Table S1 suggest that the isotherms best fit when the Langmuir equation is applied for the adsorption of rhodamine B. Comparing the q_m values, Si-MCM-48 has a higher maximum adsorption capacity (8.5×10^{-4} mol/g) than Ti-MCM-48-10 (4.6×10^{-4} mol/g). This may be ascribed to the incorporation of titania species that reduce the surface area and pore volume, thereby effectively lowering the number of adsorption sites in Ti-MCM-48-10 compared to Si-MCM-48.

The materials, Si-MCM-41 and Ti-MCM-41-10, exhibit marginally lower adsorption capacities of 8.2×10^{-4} mol/g and 4.1×10^{-4} mol/g, respectively, in comparison to Si-MCM-48 and Ti-MCM-48-10, and the results are shown in Table 1. The relatively lower adsorption capacities of rhodamine B on MCM-41 materials compared to their MCM-48 counterparts is due to the lower surface areas and pore volumes of the MCM-41 based mesoporous materials. The non-linear curve fittings for Si-MCM-41 and Ti-MCM-41-10 are illustrated in Fig. 7.

The dye molecules may adsorb on the mesoporous materials through electrostatic, non-polar, $n-\pi$, hydrogen, and covalent bonding interactions. In general, the effective adsorption sites on Si-MCM-48/41 and Ti-MCM-48/41-10 surfaces are composed mainly of OH and/or oxygen bridges ($-\text{Si}-\text{O}-\text{Si}-$ bridges). The working pH of the suspensions containing all the mesoporous materials was

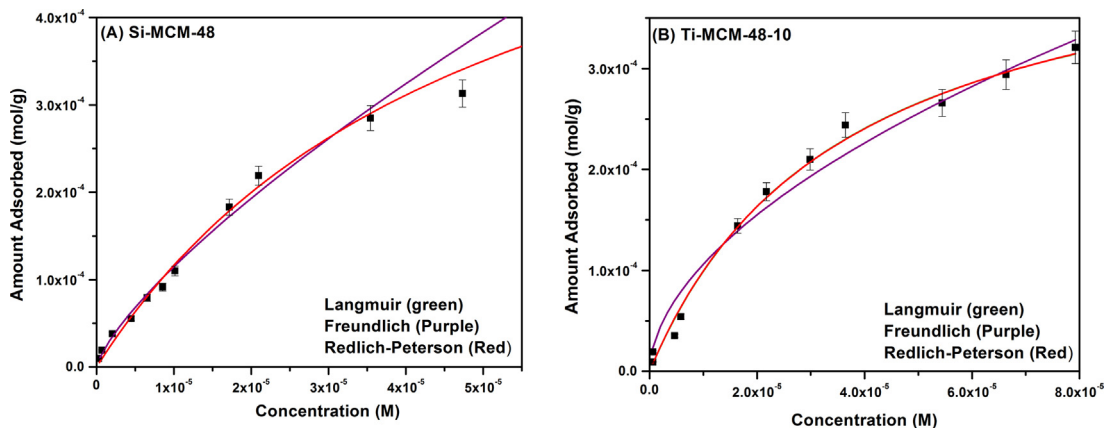


Fig. 6. Non-linear fit for the adsorption of rhodamine B on (A) Si-MCM-48 and (B) Ti-MCM-48-10.

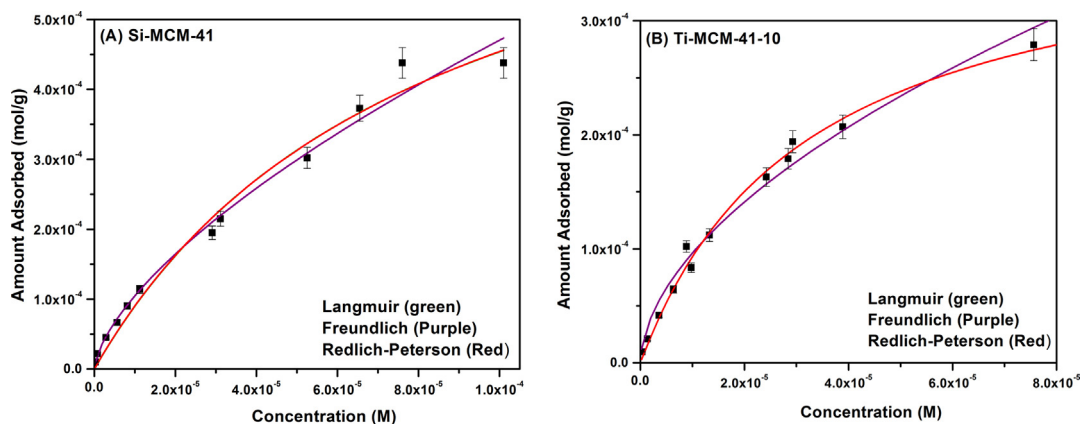


Fig. 7. Non-linear fit for the adsorption of rhodamine B on (A) Si-MCM-41 and (B) Ti-MCM-41-10.

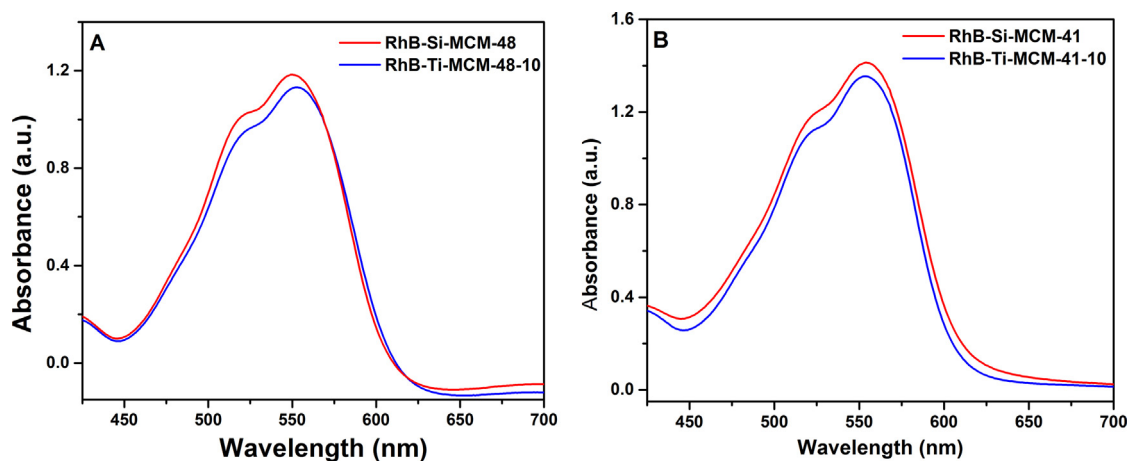


Fig. 8. The DRS spectra of the rhodamine B adsorbed on (A) MCM-48 and (B) MCM-41 materials.

found to be between 5 and 6. At this pH values, the zeta potential of Si-MCM-48, Ti-MCM-48-10, Si-MCM-41 and Ti-MCM-41-10 were found to be -4.4 , -7.6 , -10.1 , and -14.3 , respectively, and hence, the surfaces of the adsorbents are slightly negatively charged (Fig. S3). The positively charged ($-C=N^+$) group in rhodamine B have a tendency to anchor onto the surface silanol and titanol groups present in the Si-MCM and Ti-MCM materials through electrostatic forces of attraction and H-bonding [42]. In addition, the surface hydroxyl groups of the mesoporous materials may also act

as centers for the adsorption of rhodamine B through H-bonding interactions with COO^- group present in the dye molecules.

In order to better understand the adsorption of rhodamine B, DRS studies were carried out. The DR spectra of the dye adsorbed materials (after dark adsorption with the 1×10^{-4} mol/L of dye solution) are shown in Fig. 8. The absorption peak near 554 nm is attributed to the monomer form of rhodamine B, while the additional absorption peak near 520 nm, is ascribed to its dimerized form [43]. Rhodamine B molecules can form H-type or J-type

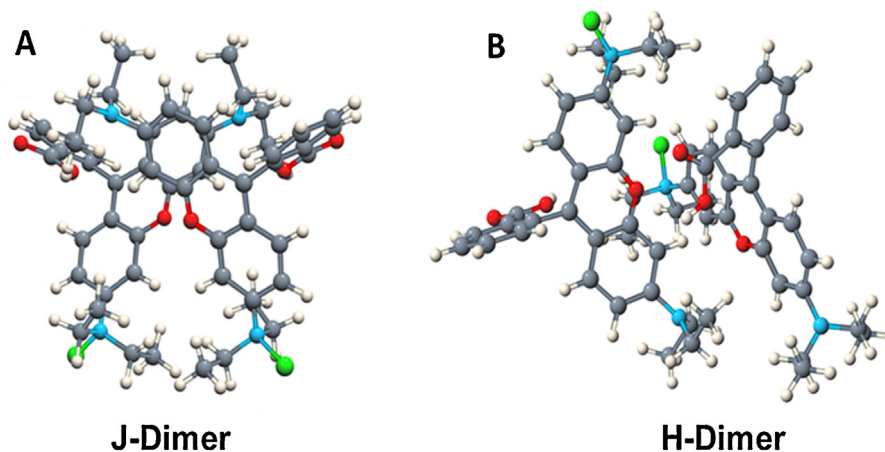


Fig. 9. The two dimerized form of rhodamine B (A) J-dimer (Two molecules are parallel to each other) and (B) H-dimer (Two molecules are perpendicular to each other).

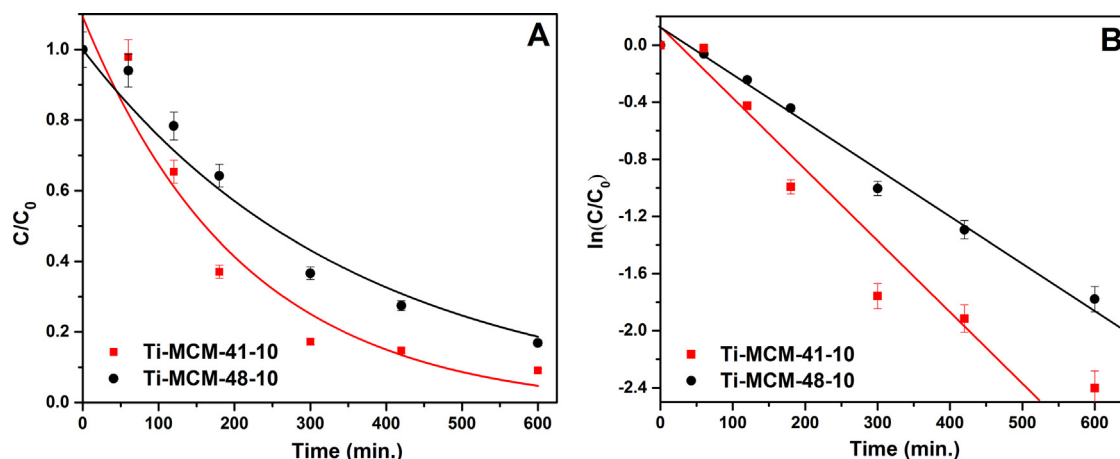


Fig. 10. Plots of (A) C_t/C_0 vs. time and (B) $\ln(C_t/C_0)$ vs. time for titania loaded mesoporous silica materials.

dimers. In order to probe this, photoluminescence studies were carried out, and Fig. S4 illustrates the photoluminescence spectra of the MCM-48 and MCM-41 mesoporous materials after adsorption of rhodamine B. Both samples show a fluorescence peak near 627 nm. The intensity of the emission from the titania loaded mesoporous materials is found to be lower and this is attributed to the weak interaction of the dimerized rhodamine B molecules with Ti^{4+} ions. The appearance of fluorescence peaks in these samples indicate the presence of J-type dimer rather than H-type dimer (shown in Fig. 9), which is non-fluorescent [44].

The results from the adsorption studies may be summarized as follows: the siliceous MCM-48 mesoporous materials in the present study show ~ 87 – 92% removal of rhodamine B in the higher concentration range from 10×10^{-5} mol/L to 50×10^{-5} mol/L and ~ 94 – 98% removal in the lower concentration range from 1×10^{-5} mol/L to 8×10^{-5} mol/L, whereas the titania loaded mesoporous materials shows ~ 78 – 89% removal in the high concentration range and ~ 90 – 94% removal in the low concentration range. Correspondingly, Si-MCM-41 mesoporous materials show ~ 81 – 90% removal of rhodamine B in the higher concentration range and ~ 93 – 98% removal in the lower concentration range, while ~ 79 – 89% removal and ~ 90 – 96% removal were obtained respectively, in the high and low concentration range with the Ti-MCM-41 materials.

Although a good adsorption profile is attained with both MCM-48 and MCM-41 materials, adsorption only transfers the dye effluent from one phase to another. Thus, in order to completely mineralize the dye molecules, photocatalytic degradation was carried out with the above mentioned titania loaded catalysts

under visible light illumination and the degradation of the titania loaded siliceous materials were compared with the corresponding siliceous materials.

3.5. Photocatalysis

The efficiency of titania loaded mesoporous silica catalysts were further examined by the degradation of rhodamine B dye under visible light irradiation. The dye solution was stirred with the catalysts in dark for 15 h to ensure complete adsorption–desorption equilibrium prior to the degradation and then the suspension was illuminated with visible light irradiation. The Ti-MCM-41-10 sample shows better degradation efficiency than Ti-MCM-48-10. The degradation of rhodamine B follows pseudo first-order kinetics as illustrated in Fig. 10, and the apparent rate constant (k_{app}) was found to be $3.17 \times 10^{-3} \text{ min}^{-1}$ for Ti-MCM-48-10, whereas Ti-MCM-41-10 showed a rate constant of $4.55 \times 10^{-3} \text{ min}^{-1}$.

The surface area of Si-MCM-41 and Si-MCM-48 are similar. On impregnation with titania, there is a decrease in the surface area. The surface area of Ti-MCM-41-10 is higher than that of Ti-MCM-48-10. The loading of titania is similar in these two materials and hence, the dispersion of titania is higher on Ti-MCM-41-10 in comparison to Ti-MCM-48-10. This is consistent with the estimation of the particle sizes. The particle size of TiO_2 was calculated using the Brus equation and was found to be 1.2 and 1.6 nm in Ti-MCM-41-10 and Ti-MCM-48-10, respectively. The higher activity of Ti-MCM-41 may also be explained by the presence of more tetrahedrally coordinated Ti^{4+} ions in Ti-MCM-41-10 than in Ti-MCM-48-10. The ratio of Ti^{4+} in octahedral/tetrahedral coordination was found to be

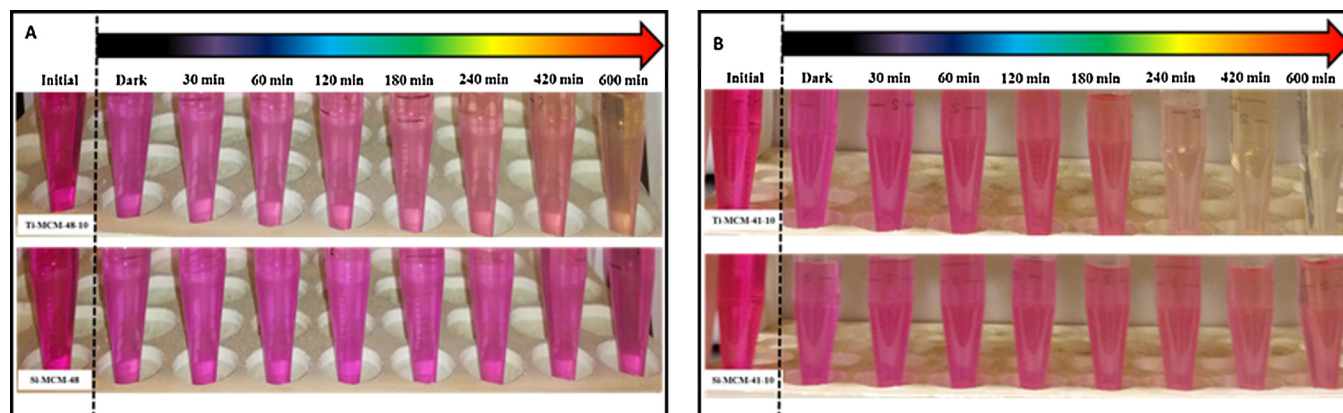
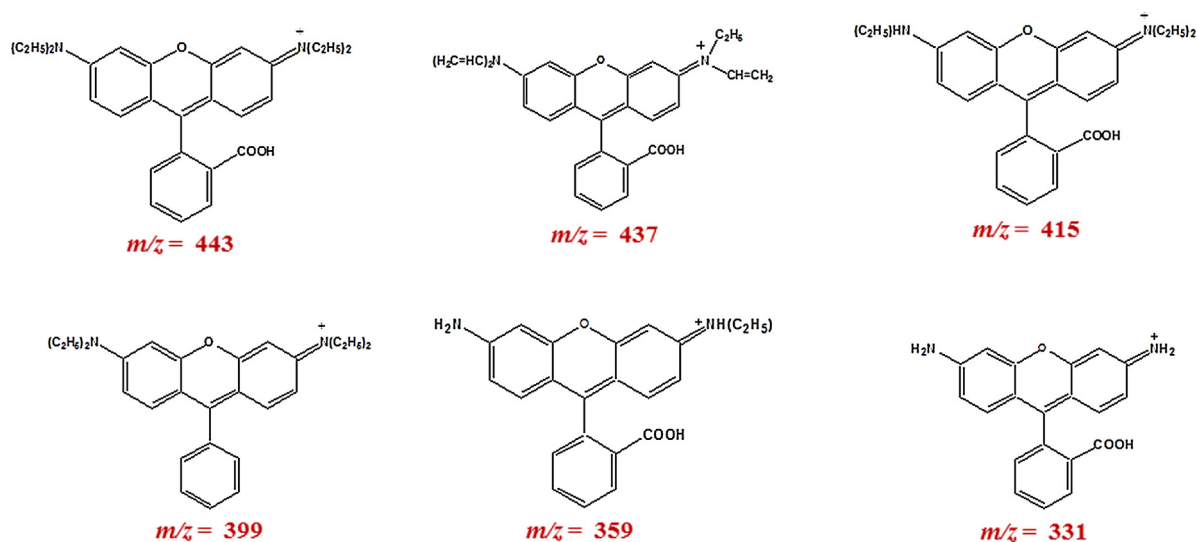
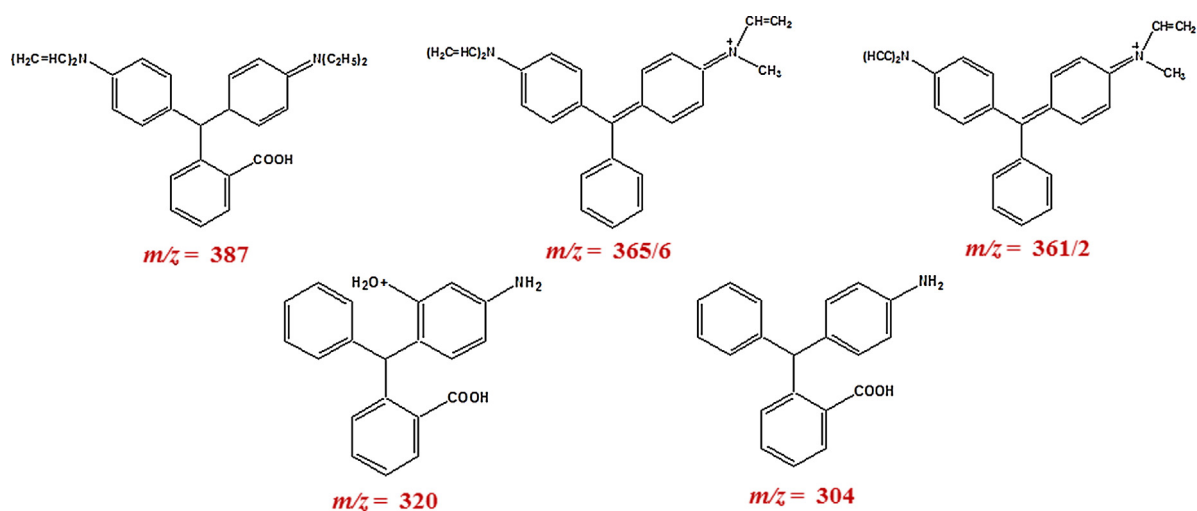


Fig. 11. The rhodamine B dye solution withdrawn at various time intervals during the degradation process for (A) MCM-48 materials and (B) MCM-41 materials.



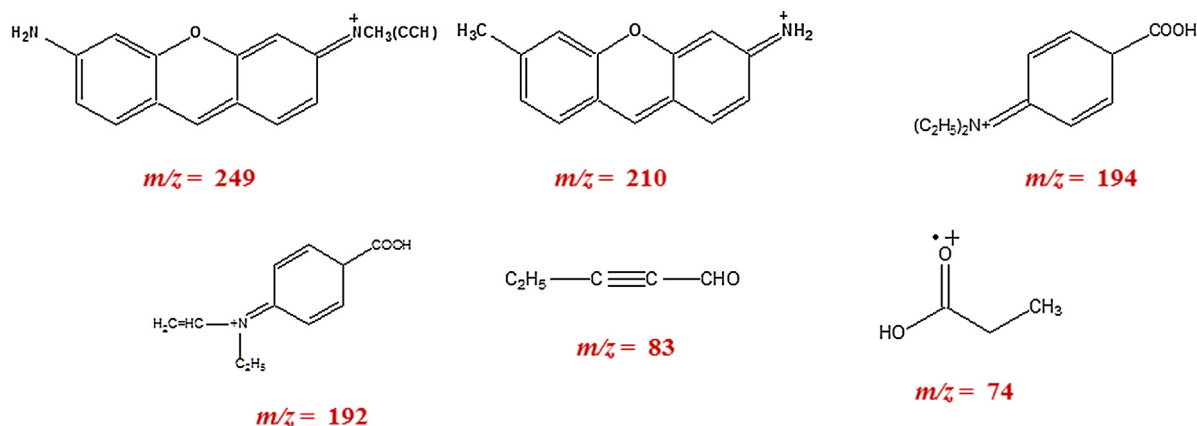
Scheme 1. Plausible intermediate products of rhodamine B molecules recorded by ESI-MS analysis.



Scheme 2. Plausible intermediates (disruption in the carbon–oxygen bond in the ring structure) of rhodamine B molecules recorded after by ESI-MS analysis.

1.65 and 2.38 for Ti-MCM-41-10 and Ti-MCM-48-10, respectively. This suggests that the activity for the degradation of rhodamine B increases with increase in amount of Ti^{4+} in tetrahedral coordination due to the formation of highly reactive photo-excited

$[\text{Ti}^{3+}-\text{O}^-]^*$ species. It has been suggested that radiation less energy transfer of the excited species given by the reverse reaction, $[\text{Ti}^{3+}-\text{O}^-]^* \rightarrow [\text{Ti}^{4+}-\text{O}^{2-}]$ takes place less efficiently in small sized titania particles with unsaturated coordination, *i.e.*, tetrahedral



Scheme 3. Plausible ring opening products of rhodamine B molecules identified by ESI-MS analysis.

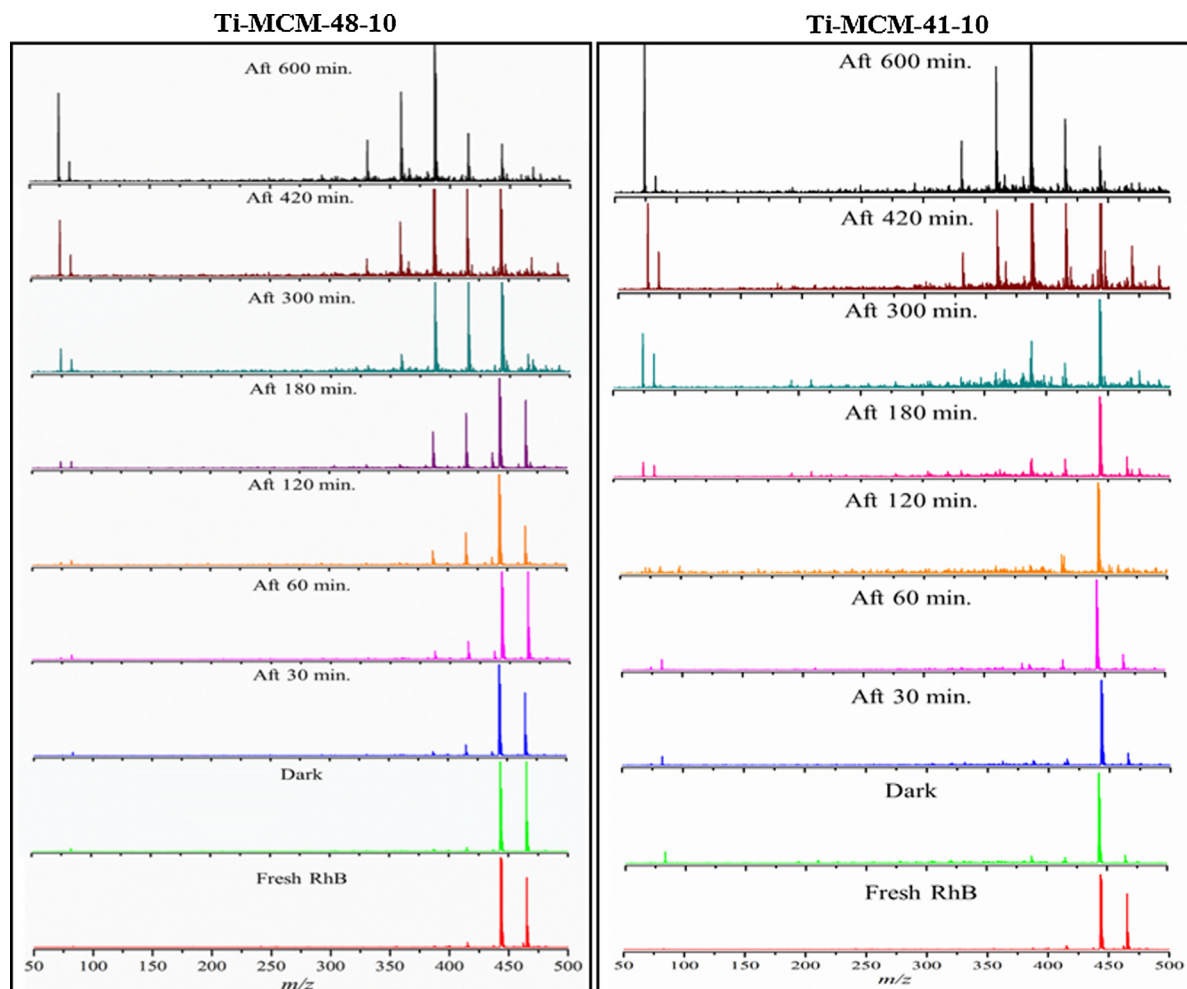


Fig. 12. The cumulative ESI-MS spectra of Ti-MCM-48-10 and Ti-MCM-41-10 against different time intervals.

coordination than in bulk titania with saturated coordination, *i.e.*, octahedral coordination of Ti^{4+} . This was expounded by us previously for solar hydrogen production [45]. Thus, the enhanced degradation of rhodamine B in Ti-MCM-41-10 is due to the relatively higher amounts of tetrahedrally coordinated Ti^{4+} ions, higher dispersion of the titania species, and the presence of smaller particle sizes of titania which leads to minimization of charge-carrier recombination in the bulk.

Although the siliceous mesoporous materials adsorbed similar amount of dye molecules, they did not show any degradation under visible light illumination. It was observed from the UV–vis studies that the absorbance maxima (λ_{max}) of rhodamine B dye solution remains relatively constant at 554 ± 3 nm during the course of degradation with Si-MCM-48 and Si-MCM-41, whereas it shifts to 449 and 443 nm during the degradation with the catalyst Ti-MCM-48-10 and Ti-MCM-41-10, respectively. This can also be clearly seen from the color of the dye solution, which was withdrawn periodically during the degradation as illustrated in Fig. 11. In particular, the color of dye solution changed from pink to relatively colorless in the presence of titania loaded MCM materials, while the solution color remained unchanged during the course of the experiment with the siliceous mesoporous materials.

The degraded products of rhodamine B formed during the visible light irradiation with the two titania loaded mesoporous materials Ti-MCM-41-10 and Ti-MCM-48-10 were identified by ESI-MS analysis. The fragmented molecular ions are detected in positive mode in the m/z range of 50–500. The degradation of xanthene type

dyes can occur via *N*-de-ethylation, de-alkylation, de-amination, de-carboxylation, de-hydration, cleavage of chromophore, and the breakage of ring structure. Two major peaks were recorded at m/z 443 and 415 for pure rhodamine B and this suggests that de-ethylation process is possible in the pure dye under our experimental conditions. However, several other fragmented peaks were also observed with different m/z values at different time intervals and the observation of these peaks validate the degradation of rhodamine B. In particular, peaks at m/z = 437 and m/z = 399 were observed with the material Ti-MCM-48-10 only. The peak at m/z = 437 was observed after 60, 120, and 180 min of visible light irradiation, whereas the peak at m/z of 399 due to de-carboxylation was observed after 120 and 180 min of visible light irradiation. The reason for the identification of these primary peaks with the Ti-MCM-48 material only may be due to its slower degradation efficiency than Ti-MCM-41 material. The faster degradation of Ti-MCM-41-10 leads to the formation of a fragment with m/z of 387 directly after de-ethylation. However, a quantitative analysis of these products could not be performed due to the commercial unavailability of these products. de-Ethylation (3 moles of C_2H_5) of the parent molecule resulted in a peak at m/z = 359, which was observed after 60 min of irradiation with Ti-MCM-48-10 and after 120 min irradiation with Ti-MCM-41-10. The peak obtained at m/z = 331 in both the samples, particularly after 300 min of irradiation is due to the complete de-ethylation (four moles of C_2H_5) from the parent rhodamine B molecule. The peaks at m/z = 443 (parent rhodamine B molecule), 437, 415, 399, 359, and 331 do not result

in any damage to the aromatic ring and the possible structures are illustrated in [Scheme 1](#). The peaks at $m/z = 387$, 365(6), 361(2), 320, and 304 were observed after the cleavage of carbon–oxygen bond in the ring structure as illustrated in [Scheme 2](#). Further cleavage in the ring structure resulted in peaks at $m/z = 249$, 210, 194, 192, 83, and 74. Particularly, the peak at $m/z = 210$ was only observed with the catalyst Ti-MCM-41-10, and the disruption in the chromophore and ring opening leads to the formation of secondary fragmented products with the m/z values of 194, 192, 83, and 74. The predicted molecular ion structures are illustrated in [Scheme 3](#). Notably, some of the fragmented species ($m/z = 366$, 362) were detected in its dually charged $[M + 2]^{2+}$ state. The changes in the intensity counts for the various peaks with time are indicated in [Fig. 12](#) for Ti-MCM-48-10 and Ti-MCM-41-10 mesoporous materials. The decrease in the intensity counts for peaks observed at relatively higher m/z values with time and the appearance of peaks with lower m/z values indicate the degradation of rhodamine B.

4. Conclusions

The adsorption of a hybrid dye, rhodamine B from aqueous solutions over two different types ordered mesoporous materials namely, MCM-48 and MCM-41 was investigated in this study. The removal efficiency of rhodamine B was found to be greater than 87% with Si-MCM-48 and 81% with Si-MCM-41 mesoporous materials, respectively, at room temperature with high concentration of dye solutions, whereas 78% and 79% of dye removal was recorded with Ti-MCM-48-10 and Ti-MCM-41-10 materials. Rhodamine B degradation was also demonstrated and the efficiency was compared among these two different ordered mesoporous materials under visible light irradiation. It was observed that the rate of degradation is dependent on the coordination of the Ti^{4+} species in the materials and the particle size of titania as well, whereas the adsorption was dependent on the surface area and the pore volume of the mesoporous materials. Also, ESI-MS studies indicate that *N*-de-ethylation, de-alkylation, de-amination, de-carboxylation, de-hydration, cleavage of chromophore, and the breakage of ring structure of rhodamine B takes place in the presence of both Ti-loaded mesoporous materials under visible light irradiation. Overall, the outcome from our studies suggests that the periodic mesoporous materials can be used as adsorbents and photocatalysts for the removal of dye molecules from aqueous solutions with high efficiency.

Acknowledgements

This work was supported by NSF-CHE-0619190, NSF-CHE-0722632, NSF-EPS-0903804, DE-EE0000270, and South Dakota Board of Regents.

Appendix A. Supplementary data

Supplementary data associated with this article can be found, in the online version, at <http://dx.doi.org/10.1016/j.apcatb.2015.02.040>.

References

- [1] T. Robinson, G. McMullan, R. Marchant, P. Nigam, *Bioresour. Technol.* 77 (2001) 247–255.
- [2] W.K. Walthall, J.D. Stark, *Environ. Pollut.* 104 (1999) 207–215.
- [3] R. Pelegrini, P. Peralta-Zamora, A.R. de Andrade, J. Reyes, N. Durán, *Appl. Catal. B* 22 (1999) 83–90.
- [4] A.H. Konsowa, M.E. Ossman, Y. Chen, J.C. Crittenden, *J. Hazard. Mater.* 176 (2010) 181–185.
- [5] S.W. Won, S.B. Choi, B.W. Chung, D. Park, J.M. Park, Y.S. Yun, *Ind. Eng. Chem. Res.* 43 (2004) 7865–7869.
- [6] Y.M. Slokar, A. Majcen Le Marechal, *Dyes Pigm.* 37 (1998) 335–356.
- [7] Y. Xu, R.E. Lebrun, P.-J. Gallo, P. Blond, *Sep. Sci. Technol.* 34 (1999) 2501–2519.
- [8] R. Ahmad, P.K. Mondal, S.Q. Usmani, *Bioresour. Technol.* 101 (2010) 3787–3790.
- [9] V.K. Gupta Suhas, *J. Environ. Manage.* 90 (2009) 2313–2342.
- [10] M.M. Nassar, M.S. El-Geundi, *J. Chem. Technol. Biotechnol.* 50 (1991) 257–264.
- [11] X. Zhuang, Y. Wan, C. Feng, Y. Shen, D. Zhao, *Chem. Mater.* 21 (2009) 706–716.
- [12] V.J.P. Poots, G. McKay, J.J. Healy, *Water Res.* 10 (1976) 1061–1066.
- [13] P. Nigam, G. Armour, I.M. Banat, D. Singh, R. Marchant, *Bioresour. Technol.* 72 (2000) 219–226.
- [14] G.S. Gupta, G. Prasad, V.N. Singh, *Water Res.* 24 (1990) 45–50.
- [15] H. Chen, A. Wang, *J. Colloid Interface Sci.* 307 (2007) 309–316.
- [16] S. Chatterjee, S. Chatterjee, B.P. Chatterjee, A.R. Das, A.K. Guha, *J. Colloid Interface Sci.* 288 (2005) 30–35.
- [17] W.L. Du, Z.R. Xu, X.Y. Han, Y.L. Xu, Z.G. Miao, *J. Hazard. Mater.* 153 (2008) 152–156.
- [18] X.Y. Huang, X.Y. Mao, H.T. Bu, X.Y. Yu, G.B. Jiang, M.H. Zeng, *Carbohydr. Res.* 346 (2011) 1232–1240.
- [19] C.T. Kresge, M.E. Leonowicz, W.J. Roth, J.C. Vartuli, J.S. Beck, *Nature* 359 (1992) 710–712.
- [20] J.S. Beck, J.C. Vartuli, W.J. Roth, M.E. Leonowicz, C.T. Kresge, K.D. Schmitt, C.T.W. Chu, D.H. Olson, E.W. Sheppard, *J. Am. Chem. Soc.* 114 (1992) 10834–10843.
- [21] D. Zhao, Y. Wan, *Chem. Rev.* 107 (2007) 2821–2860.
- [22] P.V. Messina, P.C. Schulz, *J. Colloid Interface Sci.* 299 (2006) 305–320.
- [23] S.B. Wang, H.T. Li, *Microporous Mesoporous Mater.* 97 (2006) 21–26.
- [24] M.A. Zanjanchi, A. Ebrahimi, Z. Alimohammadi, *Opt. Mater.* 29 (2007) 794–800.
- [25] P. Monash, G. Pugazhenth, *Korean J. Chem. Eng.* 27 (2010) 1184–1191.
- [26] Y.L. Dong, B. Lu, S.Y. Zang, J.X. Zhao, X.G. Wang, Q.H. Cai, *J. Chem. Technol. Biotechnol.* 86 (2011) 616–619.
- [27] C.H. Huang, K.P. Chang, H.D. Ou, Y.C. Chiang, C.F. Wang, *Microporous Mesoporous Mater.* 141 (2011) 102–109.
- [28] C.H. Huang, K.P. Chang, H.D. Ou, Y.C. Chiang, E.E. Chang, C.F. Wang, *J. Hazard. Mater.* 186 (2011) 1174–1182.
- [29] M.A. Zanjanchi, H. Sajjadi, M. Arvand, A. Mohammad-Khah, B. Ghalami-Chooobar, *Clean Soil Air Water* 39 (2011) 1007–1013.
- [30] C. Zubieta, M.B. Sierra, M.A. Morini, P.C. Schulz, L. Albertengo, M.S. Rodriguez, *Colloid Polym. Sci.* 286 (2008) 377–384.
- [31] P. Monash, G. Pugazhenth, *Adsorpt. J. Int. Adsorpt. Soc.* 15 (2009) 390–405.
- [32] X.B. Wu, K.N. Hui, K.S. Hui, S.K. Lee, W. Zhou, R. Chen, D.H. Hwang, Y.R. Cho, Y.G. Son, *Chem. Eng. J.* 180 (2012) 91–98.
- [33] P.A. Deshpande, S. Polisetti, G. Madras, D. Jyothi, S. Chandrasekaran, *Aiche J.* 58 (2012) 2987–2996.
- [34] L.H. Tian, H.T. Liu, Y. Gao, *Kinet. Catal.* 53 (2012) 554–559.
- [35] S. Anandan, *Dyes Pigm.* 76 (2008) 535–541.
- [36] A. Bhattacharyya, S. Kawi, M.B. Ray, *Catal. Today* 98 (2004) 431–439.
- [37] D. Jyothi, P.A. Deshpande, B.R. Venugopal, S. Chandrasekaran, G. Madras, *J. Chem. Sci.* 124 (2012) 385–393.
- [38] T.H. Liou, B.C. Lai, *Appl. Catal. B* 115 (2012) 138–148.
- [39] B. Boote, H. Subramanian, K.T. Ranjit, *Chem. Commun.* (2007) 4543–4545.
- [40] R. Peng, D. Zhao, N.M. Dimitrijevic, T. Rajh, R.T. Koodali, *J. Phys. Chem. C* 116 (2011) 1605–1613.
- [41] D. Zhao, S. Budhi, A. Rodriguez, R.T. Koodali, *Int. J. Hydrogen Energy* 35 (2010) 5276–5283.
- [42] F. Chen, J. Zhao, H. Hidaka, *Int. J. Photoenergy* 05 (2003) 209–217.
- [43] J. Ghasemi, A. Niazi, M. Kubista, *Spectrochim. Acta: Part A* 62 (2005) 649–656.
- [44] F. del Monte, D. Levy, *J. Phys. Chem. B* 102 (1998) 8036–8041.
- [45] C.-M. Wu, R. Peng, N.M. Dimitrijevic, T. Rajh, R.T. Koodali, *Int. J. Hydrogen Energy* 39 (2014) 127–136.